APPLIED SCIENCES AND ENGINEERING

Rapid and comprehensive detection of viral antibodies and nucleic acids via an acoustofluidic integrated molecular diagnostics chip: AIMDx

Jiao Qian[1]†, Jianping Xia[1]†, Samantha Chiang[2], Jessica F. Liu[3], Ke Li[1], Feng Li[2], Fang Wei[2], Mohammad Aziz[2], Yong Kim[2], Vinson Go[4], James Morizio[4], Ruoyu Zhong[1], Ye He[1], Kaichun Yang[1], Otto O. Yang[5], David T. W. Wong[2], Luke P. Lee[6,7,8,9,10]*, Tony Jun Huang[1]*

Precise and rapid disease detection is critical for controlling infectious diseases like COVID-19. Current technologies struggle to simultaneously identify viral RNAs and host immune antibodies due to limited integration of sample preparation and detection. Here, we present acoustofluidic integrated molecular diagnostics (AIMDx) on a chip, a platform enabling high-speed, sensitive detection of viral immunoglobulins [immunoglobulin A (IgA), IgG, and IgM] and nucleic acids. AIMDx uses acoustic vortexes and Gor'kov potential wells at a 1/10,000 subwavelength scale for concurrent isolation of viruses and antibodies while excluding cells, bacteria, and large (>200 nanometers) vesicles from saliva samples. The chip facilitates on-chip viral RNA enrichment, lysis in 2 minutes, and detection via transcription loop–mediated isothermal amplification, alongside electrochemical sensing of antibodies, including mucin-masked IgA. AIMDx achieved nearly 100% recovery of viruses and antibodies, a 32-fold RNA detection improvement, and an immunity marker sensitivity of 15.6 picograms per milliliter. This breakthrough provides a transformative tool for multiplex diagnostics, enhancing early infectious disease detection.

INTRODUCTION

Historically, every decade has seen the emergence of a new pandemic (*1*, *2*). Recent examples include severe acute respiratory syndrome coronavirus (SARS-CoV) in 2002, H1N1 influenza in 2009, and the novel coronavirus SARS-CoV-2 in 2019 (COVID-19) (*3*, *4*). Not only do these virulent diseases compromise global health through a heavy burden of infections and fatalities, but they also strain public health infrastructures and economies. This underscores the urgent need for rapid, cost-effective, and efficient diagnostic tools. Precise diagnosis and monitoring of infections (*5*, *6*) pave the way for implementing timely infection control measures, targeted and effective isolation policies, and appropriate medical care.

Currently, the forefront of diagnostic strategies for emerging pandemic diseases includes nucleic acid testing (*7*–*10*), antigen testing (*11*–*13*), and antibody testing (*14*–*16*). Each of these diagnostic methodologies offers a distinct perspective on the presence of infection or the status of immunity, offering a comprehensive overview of disease spread and population health impact. Nucleic acid testing strategies search for the presence of pathogens' genetic material using polymerase chain reaction (PCR) technology. Although PCR is sensitive and specific, it requires trained personnel and extensive lab equipment (*17*), limiting its use for point-of-care diagnostics. Antigen tests identify specific viral surface proteins and are rapid, cost-effective, and applicable at the point of care; however, they often lag behind PCR in accuracy and sensitivity (*18*). Last, antibody tests identify antibodies that have already formed against pathogens. Thus, they rely on the development of a host immune response. Because this process of antibody formation after infection can take 1 to 3 weeks (*19*), the use of antibody tests for early detection is limited.

Nucleic acid, antigen, and antibody testing each provide valuable information regarding the spread of pathogens and the host immune response. Combining these technologies would offer an even more comprehensive view of the containment and spread of novel infectious diseases. Unfortunately, integrated comprehensive diagnostic testing using these methods remains a complex endeavor that necessitates high-cost equipment and notable labor requirements, which must be widely deployed across various laboratories and hospitals to be effective at the population level.

Consolidating numerous laboratory procedures onto a single chip streamlines and expedites testing (*20*–*22*). Key innovations in this realm, including microfluidic PCR chips (*23*–*25*), CRISPR-based chips (*26*, *27*), and electrochemical sensing chips (*28*–*30*), warrant special attention. These automated on-chip sensing technologies stand out for their ability to provide vital diagnostic insights with minimal labor and specialized expertise. Furthermore, notable progress has been made in integrating nucleic acid detection and immunoglobulin G (IgG) detection, opening the door for in-depth analyses of infection and immunity profiles (*29*). Unfortunately, despite these advances, off-chip sample prepurification steps such as centrifugation (*31*) and filtration (*32*, *33*) are often required to attain high sensitivity and low detection limits. A range of on-chip methods (*34*–*36*) are under investigation to address this issue, including using magnetic beads (*37*–*39*), acoustofluidic separation

[1]Thomas Lord Department of Mechanical Engineering and Materials, Duke University, Durham, NC 27708, USA. [2]School of Dentistry, University of California Los Angeles, Los Angeles, CA 90095, USA. [3]Department of Anesthesiology, Duke University, Durham, NC 27710, USA. [4]Department of Electrical and Computer Engineering, Duke University, Durham, NC 27710, USA. [5]Division of Infectious Diseases, Department of Medicine, David Geffen School of Medicine, University of California, Los Angeles, Los Angeles, CA 90095, USA. [6]Renal Division and Division of Engineering in Medicine, Department of Medicine, Brigham and Women's Hospital, Harvard Medical School, Harvard University, Boston, MA 02115, USA. [7]Department of Bioengineering, University of California, Berkeley, Berkeley, CA 94720, USA. [8]Department of Electrical Engineering and Computer Science, University of California, Berkeley, Berkeley, CA 94720, USA. [9]Department of Biophysics, Institute of Quantum Biophysics, Sungkyunkwan University, Suwon 16419, Korea. [10]Department of Chemistry and Nano Science, Ewha Womans University, Seoul 03760, Korea.
*Corresponding author. Email: lplee@bwh.harvard.edu (L.P.L.); tony.huang@duke.edu (T.J.H.)
†These authors contributed equally to this work.

(*40*–*47*), ultrafiltration (*48*, *49*), chromatography (*50*, *51*), and spiral microfluidic channels (*52*, *53*). However, these techniques risk unintentionally eliminating vital biomarkers like immunoglobulin A (IgA) in the purification process. Consequently, obtaining a comprehensive dataset encompassing viral RNA, host immunity antibodies (including IgA, IgM, and IgG), and disease antigens continues to be a notable challenge, primarily because of the low concentrations of these substances in patient samples.

In this work, we report an acoustofluidic integrated molecular diagnostics (AIMDx) chip that enables efficient and concurrent detection of immunoglobulins (IgA, IgG, and IgM) and viral nucleic acids and achieves rapid, sample-to-answer, high-sensitivity diagnostics. The point-of-care AIMDx chip comprises a sample purification module, a viral lysis-RNA detection module, and an antibody detection module. The sample purification module features a serpentine microchannel with acoustically oscillating wedge structures. Because of the acoustic streaming vortexes (*54*) and subwavelength (1/10,000 λ), the Gor'kov potential well that emerges around the tip of each wedge structure results in cells, bacteria, and microvesicles from saliva being effectively trapped. Meanwhile, antibodies and viruses are separated from mucoprotein and remain suspended in the fluid, facilitating the purification of the saliva sample for optimized downstream biosensing. The viral lysis-RNA detection module combines purified saliva with a buffer to ensure the swift release of viral RNA in under 2 min. A high-sensitivity detection module follows this to identify multiple target RNA genes simultaneously. Last, the antibody detection module offers a comprehensive early assessment of key antibodies, including IgG, IgM, and the frequently overshadowed IgA, often camouflaged by mucin protein. Notably, our integrated on-chip purification method enhances RNA detection sensitivity by 32-fold compared to raw samples and reduces the antibody detection threshold from 2 ng/ml to a mere 15.6 pg/ml. Our AIMDx chip sets the stage for a swift, noninvasive, ultrasensitive methodology for sample preparation and simultaneous RNA and antibody detection. This innovative approach opens the door to rapidly testing the efficacy of targeted vaccines and treatment blueprints, enhancing our ability to navigate and neutralize pandemics.

RESULTS

Design and workflow of the point-of-care AIMDx device

Saliva samples are preferred for medical diagnostics because of their richness in crucial biomarkers, such as host immunity antibodies, neutralizing antibodies, and various infectious and viral markers (Fig. 1A). Saliva sampling offers multiple advantages over blood sampling: Saliva can be collected with minimal invasiveness, usually requires a smaller volume for downstream diagnostic applications, and allows for simple tube-based collection, eliminating the need

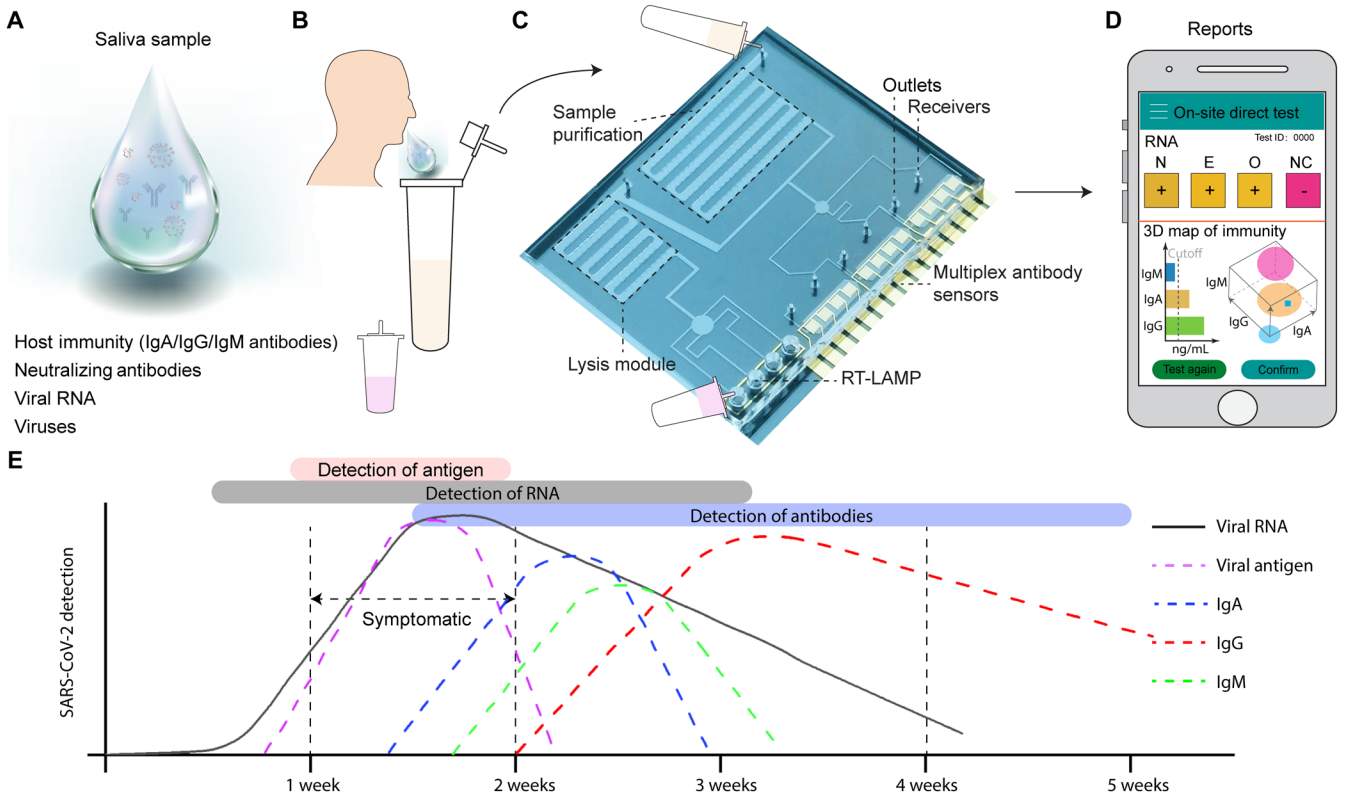

Fig. 1. Workflow of the AIMDx chip. (**A**) Saliva samples contain key biomarkers such as host immunity antibodies, neutralizing antibodies, viral genetic material, and virus particles. (**B**) Procedure for self-directed saliva sample collection and RT-LAMP mixture preparation. (**C**) Image of the integrated AIMDx chip, highlighting its four primary modules: sample purification, viral lysis, RNA detection, and antibody detection. (**D**) Comprehensive detection report: It presents the colorimetric outcomes of RT-LAMP assays for three target RNA genes, contrasted with a negative control, and quantifies antibody levels for IgM, IgA, and IgG. The report also features a three-dimensional (3D) view of the complete range of host antibodies. (**E**) Timeline for detecting SARS-CoV-2 using nucleic acid, antigen, and antibodies (IgA, IgM, and IgG) tests, adapted from published work (*57*).

for skilled health care professionals for collection (Fig. 1B). This feature makes saliva an attractive and promising clinical specimen for point-of-care diagnostics. However, saliva often contains a higher concentration of nonbiomarker elements than blood. Consequently, saliva samples require off-chip purification to remove cells, bacteria, large microvesicles, and other waste materials. Our device addresses this challenge by integrating both purification and detection functionalities on a single chip. As illustrated in Fig. 1C, the comprehensive portable AIMDx device comprises four main modules: (i) sample purification, (ii) viral lysis, (iii) RNA detection, and (iv) antibody detection. First, the purification and lysis modules consist of polydimethylsiloxane (PDMS) microfluidic channels with acoustically oscillating wedge microstructures. Next, the RNA detection module comprises a PDMS microchannel housing four wells that receive pre-prepared reverse transcription loop–mediated isothermal amplification (*55*, *56*) (RT-LAMP) reagents (Fig. 1B, depicted in red). Last, the antibody detection module comprises three PDMS chambers with inlets and outlets that facilitate the flow of detection reagents.

In addition, the glass substrate hosts three groups of electrochemical sensors aligned with the chambers, enabling the detection of IgA, IgG, and IgM antibodies. Additional design details and the parameters of the PDMS microchannels and sensors are described in Materials and Methods and in fig. S1. After the collected saliva sample is loaded into the inlet of the device, it passes through the purification and lysis modules to reach the detection zone. Here, RT-LAMP and electrochemical sensing technologies identify RNA and antibody moieties of interest. Ultimately, a detailed detection report is provided to the patient, encompassing colorimetric RT-LAMP outputs for three target RNA genes, as well as quantitative levels of antibodies, including IgM, IgA, and IgG (Fig. 1D). In addition, a three-dimensional representation detailing the full spectrum of host antibodies is presented, offering a visual depiction of the patient's immune profile to monitor the patient's immune response more effectively. At present, various detection technologies for nucleic acids, antigens, and antibodies are used at different stages of infection (*57*). Unlike previous methods, the developed AIMDx chip offers comprehensive information about viral RNA, antigen, and antibody levels at various stages of the disease process, ranging from early infection to recovery (Fig. 1E).

Mechanism and performance of the sample AIMDx purification module for saliva samples

The sample purification module of the AIMDx chip features wedge microstructures within a PDMS microfluidic channel that is acoustically excited using an acoustic buzzer bonded to the device's glass substrate. At its resonant frequency of 5 kHz, the buzzer induces vibrations in the glass substrate, leading to oscillations in the wedges. Crucially, the dimensions of the wedges range from 2 μm at their narrowest edge to 200 μm at the widest, notably smaller than the 30-cm acoustic wavelength (λ) in the fluid. Despite their small size, they notably alter the acoustic vibration velocity in their vicinity. This acoustic vibration velocity fluctuates in the vicinity of a wedge yet remains relatively stable in regions further from the wedge, leading to a notably subwavelength Gor'kov potential well that measures just 1/10,000 λ in diameter (Fig. 2A). The gradient variations in Gor'kov potential generate a substantial acoustic radiation force (*58*) capable of manipulating bioparticles as small as 200 nm. Figure 2B illustrates the acoustic vibration velocity: High acoustic vibration velocity is observed near each microwedge, leading to pronounced acoustic streaming. Simulations of the acoustic streaming pattern within the device show two counter-rotating acoustic streaming vortexes around the tip of each wedge (Fig. 2C). The resulting acoustic streaming drag force causes bioparticles to rotate within the streaming vortex. Simultaneously, the subwavelength Gor'kov potential well introduces an acoustic radiation force, pushing bioparticles toward the center of the vortex. This robust acoustic streaming also effectively separates IgA from mucoprotein, rendering it detectable by downstream analytical tools. Therefore, as saliva samples were introduced into the purification module of the microchannel, larger cells and microvesicles were effectively captured in the vortex centers. At the same time, smaller antibodies and viruses proceeded downstream (Fig. 2D). By using a low-frequency acoustic chip to capture nanometer-scale bioparticles, our approach eliminates the need for bulky radio-frequency power amplifiers and function generators. This makes the chip suitable for point-of-care applications.

To visualize the acoustic streaming in the AIMDx chip, green fluorescent polystyrene particles with a diameter of 500 nm were introduced into the microfluidic channel. The particle trajectories are plotted in Fig. 2E by overlapping images over time and show a similar acoustic streaming pattern to that predicted by the simulation results in Fig. 2C. Notably, one of the acoustic vortices that aligns with the background fluid flow around each wedge structure is suspended, likely because of the presence of air bubbles at the sharp edges of the wedges. These air bubbles modify the acoustic streaming pattern, resulting in a dominant vortex that opposes the background flow (movie S1). To visualize the acoustic trapping (*59*–*61*) of large particles, we further introduced 1-μm-diameter green, fluorescent polystyrene particles into the microfluidic channel. As shown in Fig. 2F, the particles were tightly confined near the tip of the wedge microstructures, while the carrier fluid continued to flow downstream within the microfluidic channel. A movie showing the dynamic trapping of microparticles is shown in movie S2. Separation of 5-μm particles from 100-nm particles via size-based differential trapping is shown in fig. S2. Movie S3 demonstrates the selective trapping of 390-nm particles while permitting the passage of smaller particles sized at 50 nm. Hence, the acoustofluidic channel patterned with wedge microstructures offers a promising approach for the effective separation of complex biofluids, which often contain biological moieties of varying size. This method removes large cells, bacteria, and microvesicles in saliva samples, resulting in purified samples containing only antibodies and viruses (fig. S3).

To assess the RNA and protein isolation capability of the AIMDx chip, we loaded raw saliva samples into the device and collected the acoustically purified sample at the output. Nanoparticle tracking analysis (NTA; Malvern, UK) was used to assess the composition of both the raw and purified saliva samples (Fig. 2, G and H, respectively). The raw (unpurified) samples consisted mostly of particles larger than 200 nm, with the majority exceeding 1 μm (Fig. 2G); conversely, following isolation, an identical volume of the acoustic purified sample exhibited particles primarily ranging from 50 to 200 nm (Fig. 2H). Centrifugation of the raw and purified samples at 16,000*g* similarly demonstrated that the raw (unpurified) sample contained a notable number of cells, debris, and microvesicles, while the acoustic purified sample did not (Fig. 2, G and H, right). Microscopy images of the raw versus AIMDx-purified saliva samples similarly demonstrate the removal of large debris (fig. S4). Collectively, these data demonstrate the successful trapping and removal of large

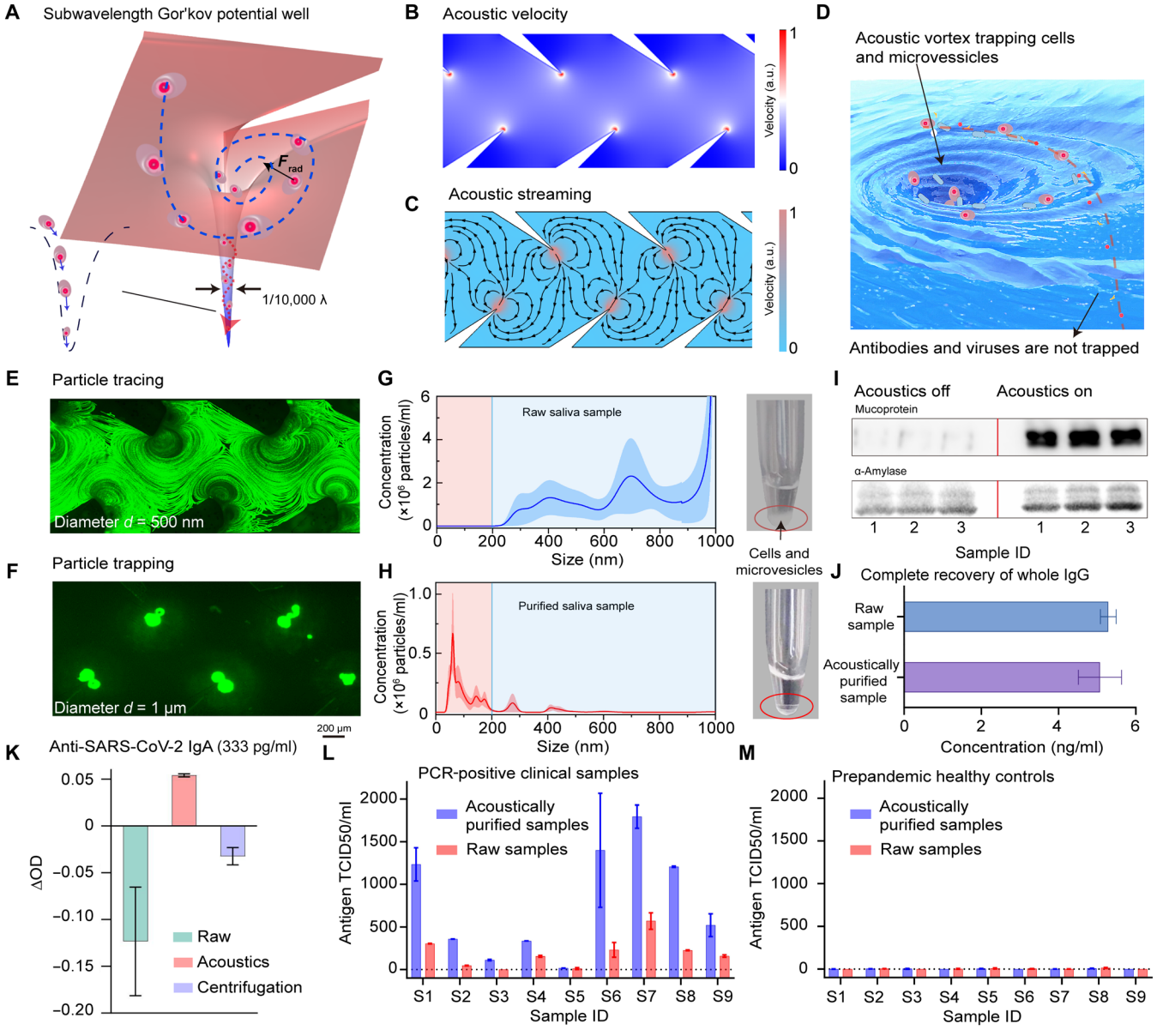

Fig. 2. Acoustically driven purification of saliva samples via AIMDx. (**A**) Visualization of the subwavelength Gor'kov potential well near a wedge microstructure, highlighting a region (d = 1/10,000 λ) with a notably reduced Gor'kov potential and a pronounced acoustic radiation force for cell and microvesicle trapping. (**B**) Illustration of the acoustic velocity distribution within the PDMS microchannel, showcasing pronounced changes in acoustic velocity near the apex of each acoustic wedge, which contributes to the notable decreases in Gor'kov potential. a.u., arbitrary units. (**C**) Simulation results showing normalized acoustic streaming velocity with two acoustic vortexes formed around each wedge tip. (**D**) Illustration depicting the acoustic trapping of cells, bacteria, and microvesicles. (**E**) Experimental trajectories of 500-nm-diameter green fluorescent polystyrene particles within the microchannel. (**F**) Observed trapping pattern of 1-μm-diameter green fluorescent polystyrene particles inside the microchannel. (**G** and **H**) Comparative size distribution of particulates in raw and purified saliva samples, as determined by NTA (n = 3). (**I**) Western blot examination comparing protein content in raw saliva samples (1, 2, and 3) to their purified counterparts. (**J**) Comparative concentration of whole IgG in raw and purified saliva samples (n = 3). (**K**) Detection level of anti-SARS-CoV-2 S1 RBD IgA antibodies in raw versus purified saliva samples (n = 3). (**L** and **M**) Comparison of measured antigen concentration between (L) acoustically purified and raw clinical (COVID-19 PCR-positive) samples and (M) prepandemic healthy control samples by off-chip electrochemical detection (n = 3).

particles and impurities from saliva samples by the sample purification module of the device.

We also verified the efficacy of protein isolation by Western blot. For this analysis, we focused on mucoprotein and α-amylase, two proteins commonly found in saliva samples. As shown in Fig. 2I, the concentration of both proteins is notably higher in the purified saliva sample than in the raw saliva sample. This difference was especially pronounced for mucoprotein. We posit that this is due to the high concentration of impurities in the original sample, which renders accurate protein detection challenging in the raw sample. Therefore, our acoustofluidic-based sample purification process successfully enhances the detection of proteins in the isolated saliva sample.

To evaluate the yield (retention) of our purification module, we measured the concentration of whole IgG in raw versus acoustically

purified samples using a standard Human IgG ELISA kit. The standard curve for whole IgG detection is shown in fig. S5. Because of its high concentration in saliva, the detection of entire IgG is highly sensitive and not affected by impurities in the sample. We found that the concentration of the whole IgG was unchanged by the on-chip acoustic purification process, indicating a near-total recovery of antibodies using our device. However, our primary interest lies in certain specific antibodies, such as the anti-SARS-CoV-2 S1 receptor binding domain (RBD) IgA antibody, as a deficiency in this antibody has been linked to increased COVID-19 severity and vaccine ineffectiveness (*62*). To investigate the ability of the chip to detect IgA, we introduced an anti-SARS-CoV-2 S1 RBD IgA antibody with a concentration of 333 pg/ml into saliva samples from healthy controls. Subsequently, we purified these samples using the sample purification module and high-speed centrifugation (16,000*g* for 15 min). As shown in Fig. 2K, the acoustically purified sample yields a positive enzyme-linked immunosorbent assay (ELISA) signal for the IgA antibody.

In contrast, the signal in the raw and centrifugation-purified samples is masked by high background noise because of nonspecific protein absorption. This result indicates that our purification technique can lower the detection threshold for rare antibodies and other pertinent biomarkers by mitigating the influence of large contaminants and small proteins in biological samples. To assess the impact of acoustic purification on antigen detection, 18 samples were analyzed: 9 from patients with COVID-19 who are PCR positive and 9 from prepandemic healthy controls. Each sample underwent on-chip acoustofluidic purification followed by off-chip electrochemical detection, and the results were compared to those of raw samples. In the PCR-positive group, eight samples showed a two- to fivefold increase in signal intensity after purification, while one sample exhibited low readings both before and after purification (Fig. 2L). In contrast, all healthy control samples consistently showed negligible readouts regardless of purification (Fig. 2M). These findings suggest that acoustofluidic purification notably enhances the detection of antigens in PCR-positive samples without affecting the readouts of control samples. The observed signal enhancement following acoustofluidic purification highlights the potential of integrating this technique with on-chip detection methods for viral biomarkers.

Improved detection by enriched multiple RNA biomarkers via local acoustofluidic lysis

To improve the capability of our portable AIMDx chip to detect multiple RNA biomarkers, we used an on-chip continuous two-step approach with an acoustofluidic lysis module and an RNA detection module. In the lysis module, we used acoustic streaming generated by the wedge microstructures to help lyse viral particles (Fig. 3A). Virus in purified saliva samples was mixed with lysis buffer (10% Tween 20) using the acoustic streaming vortices (Fig. 3A, solid purple lines), resulting in near-immediate viral lysis and RNA release. To evaluate lysis performance, we first varied sample processing time. To this end, we introduced a pellet of pure inactivated SARS-CoV-2 whole virus (no. 76460-364, VWR, US) in 100 μl of 0.1× tris-acetate-EDTA (TAE) buffer (no. B49, Thermo Fisher Scientific, US) in molecular standard water into the device. The virus sample was passed through the lysis module both with and without acoustics; processing time (resident time in the chamber) was determined by adjusting the sample flow rate through the channel. The particle concentration of the collected sample at the outlet was quantified by NTA. Nearly half of the viral particles remained intact without acoustofluidic lysis after 20 min of processing. In contrast, acoustofluidic lysis effectively processed almost all of the viral sample in just 2 min (Fig. 3B). To further visualize the effects of acoustofluidic lysis, we captured transmission electron microscopy (TEM) images of the purified virus sample with and without acoustics for 2 min. Numerous viral particles were visualized without acoustics on TEM; in contrast, after acoustofluidic lysis, viral debris was visualized with few intact viruses (Fig. 3C).

Meanwhile, the RNA detection module comprises four wells designed for the detection of targeted genes via RT-LAMP technology (Fig. 3D). These wells detect (i) the nucleocapsid gene of SARS-Cov-2 (N), (ii) open reading frame 1a of SARS-CoV-2 (O), (iii) the envelope gene of SARS-CoV-2 (E), and (iv) a negative control (NC). All necessary RT-LAMP reagents were premixed to mitigate the risk of contamination and subsequent false-positive results associated with multiple manual sample handling steps. To ensure simultaneous detection across the four wells, auxiliary microfluidic channels were incorporated into the RNA detection module to allow simultaneous sample loading into all four wells (fig. S6). After purified and lysed saliva samples were loaded, the pre-prepared RT-LAMP mix reagents (initially pink) were directly added to their corresponding wells. A thermoelectric cooler (Amazon, TEC126306) was used to achieve the required temperature (65°C) for the reaction. Thermal profiling of the colorimetric RT-LAMP reagent upon exposure to the thermoelectric cooler is shown in fig. S7. After incubation at 65°C for 30 min, the final solution color was observed: Yellow indicated a positive result, while pink indicated a negative outcome. In this study, raw saliva samples spiked with inactivated SARS-CoV-2 virus and healthy saliva samples were tested. An image of RT-LAMP results for a sample containing SARS-CoV-2 viral particles is shown in Fig. 3E: As expected, the wells corresponding to the targeted genes (SARS-CoV-2 genes N, O, and E) demonstrated a colorimetric change, while the negative control did not. In contrast, all four wells showed no colorimetric healthy saliva shift samples. This colorimetric change is quantified in fig. S8.

To validate the effect of acoustofluidic purification on viral RNA detection, we processed two symptomatic clinical samples with the developed AIMDx chip to perform integrated sample purification, viral RNA extraction, and on-chip RT-LAMP. The two samples were then transferred to an off-chip electrochemical-based viral RNA detection platform (described in Materials and Methods). The same two symptomatic samples were also directly lysed and analyzed by RT-LAMP off-chip, followed by the electrochemical detection process for viral RNA. The negative (water) and positive control (pure target RNA) results are plotted for reference. As shown in Fig. 3F, the acoustically treated samples show a nearly fivefold increase in electrochemical signal compared with the untreated (no acoustics) group. We therefore conclude that acoustic removal of the inhibitors in the saliva samples enhances the RT-LAMP reaction, allowing for a higher signal from electrochemical detection.

As described above, acoustofluidic-based sample purification plays a crucial role in enhancing the sensitivity of multiplex RNA detection by removing large impurities from saliva samples. To demonstrate the impact of this purification on RNA detection performance using the on-chip colorimetric method, we serially diluted inactivated SARS-CoV-2 virus into raw saliva samples. In Fig. 3 (G to I), we characterize the detection limit of our integrated AIMDx chip for each of the three gene regions of interest (N, O, and E)

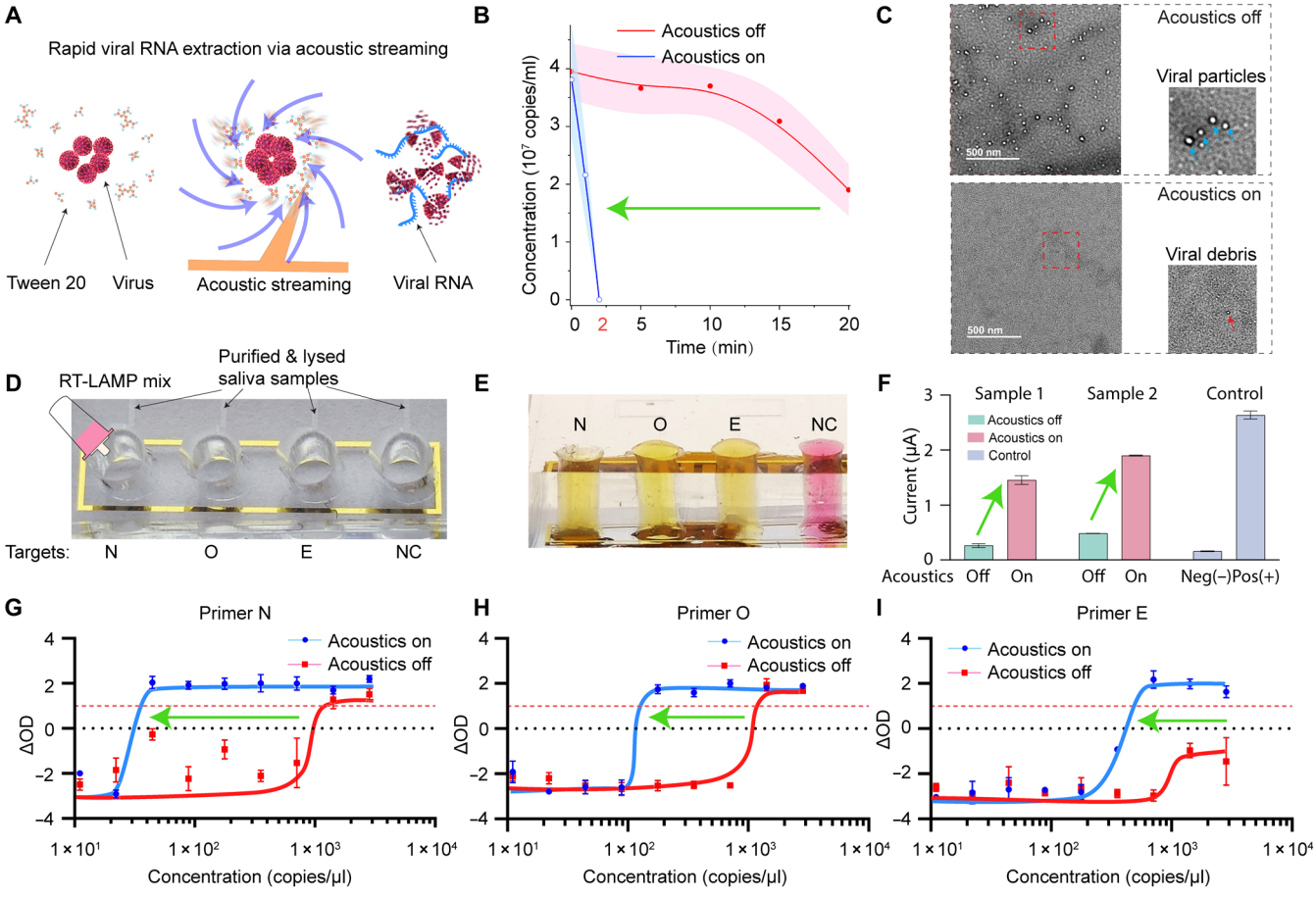

Fig. 3. On-chip acoustofluidic lysis of viral particles and detection of multiplex RNA biomarkers using the AIMDx chip. (**A**) Mechanism of acoustically driven, on-chip viral lysis. (**B**) Concentration of viral particles as a function of processing time in the acoustofluidic lysis module both with and without acoustics, as measured by NTA ($n = 3$). Without acoustics, ~50% of particles are lysed at 20 min. With acoustic enhancement, nearly all viruses are lysed within 2 min. (**C**) TEM images of purified saliva samples before and after acoustofluidic lysis. Inset (right): magnified view of boxed area. (**D**) Image of RNA detection module. (**E**) Image of colorimetric RT-LAMP results for a sample containing SARS-CoV-2 viral particles. (**F**) Electrochemical detection of RT-LAMP–amplified clinical samples shows signal enhancement in acoustically purified samples compared to raw (unpurified) samples. (**G** to **I**) Detection limit of the integrated chip for the three gene regions N, O, and E of SARS-CoV-2 with and without acoustofluidic isolation ($n = 4$).

of SARS-CoV-2, both with and without acoustofluidic purification. With a "positive" result threshold of $\Delta OD = 1$, we demonstrated an eightfold improvement in the detection limit for all three queried SARS-CoV-2 genes using the integrated chip. In particular, the viral RNA detection limit of the N gene was improved 32-fold in treated versus untreated saliva samples, with a limit of detection (LOD) of ~44 copies/μl. The enhanced sensitivity after acoustofluidic purification likely arises from improved primer-target binding because of inhibitor removal, with the N gene showing the greatest amplification efficiency because of its optimized primers and stable RNA structure. These data demonstrate that our integrated AIMDx chip enables high-sensitivity multiplex detection of RNA biomarkers from saliva samples without the need for off-chip preprocessing.

Improved simultaneous detection of multiple SARS-CoV-2 antibodies via AIMDx

In addition to multiplex RNA biomarker detection, our AIMDx chip can achieve multiplex antibody (anti-SARS-CoV-2 S1 RBD IgG/IgM/IgA) detection from raw saliva samples. While on-chip detection of anti-SARS-CoV-2 S1 RBD IgG has been documented, on-chip detection of IgA remains a challenge. IgA often coexists with saliva mucin proteins (*63*), potentially inhibiting its detection using on-chip techniques. However, acoustofluidic purification offers a promising solution. Strong acoustic streaming forces can dissociate IgA from the complex environment dominated by mucin proteins (*63*), rendering IgA detectable by most on-chip detection methods (Fig. 4A). Unlike typical methods that require an off-chip purification step and a standard electrochemical sensing working station, our device combines the sample purification module with electrochemical sensors for antibody detection (Fig. 4B). Three detection units are used to detect IgA, IgG, and IgM antibodies. To ensure simultaneous detection across the chambers, we designed auxiliary microfluidic channels to allow the sample to flow into each chamber at a consistent velocity (see fig. S6). A schematic showing a single detection unit comprising four electrochemical sensors is shown in Fig. 4C. Three sensors are coated with SARS-CoV-2 spike protein RBD for repeated measurements. In contrast, the fourth sensor is uncoated and is a negative control. In this schema, the working electrodes of the four sensors are

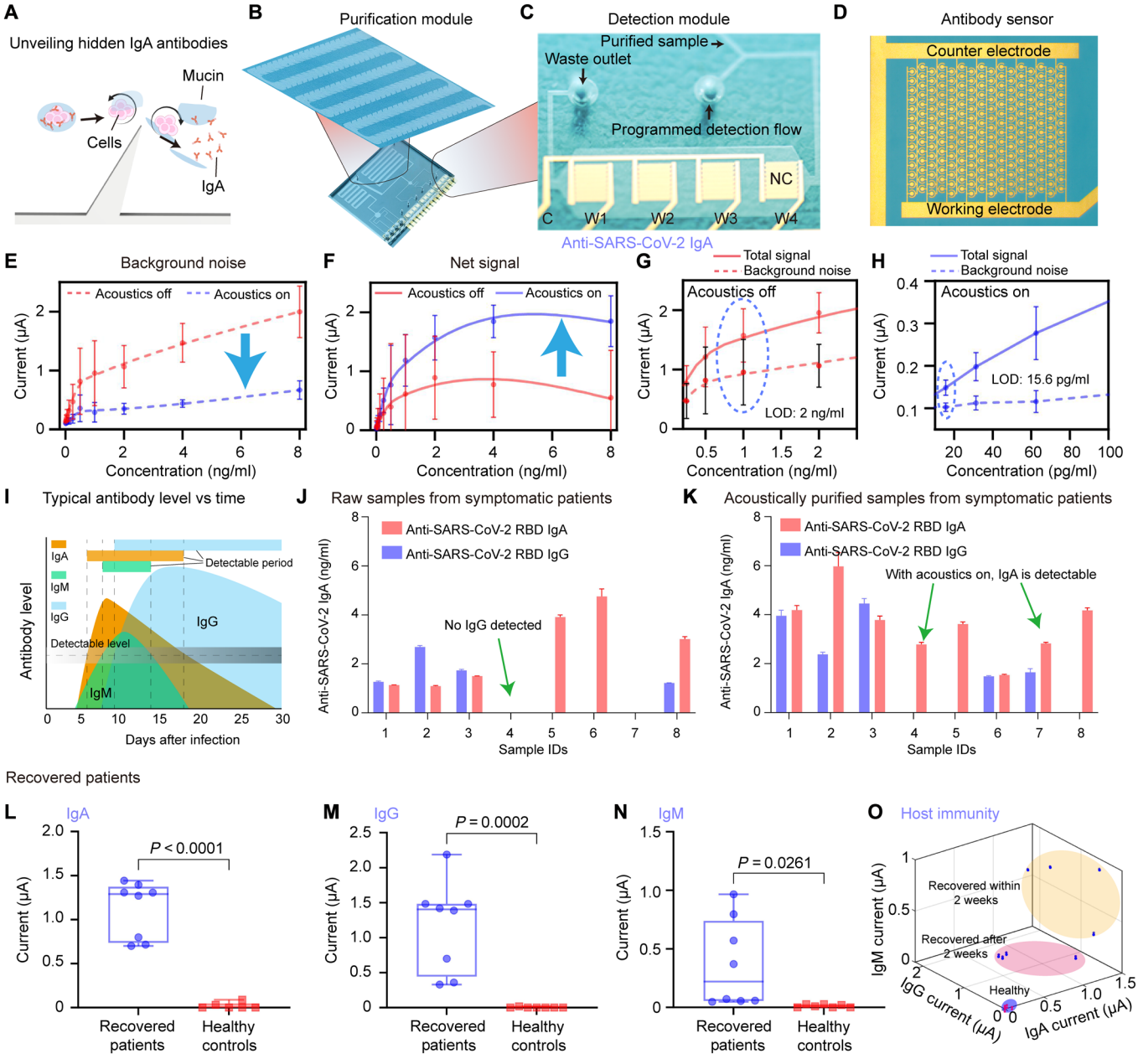

Fig. 4. Detection performance of the AIMDx chip for multiple SARS-CoV-2 antibodies. (**A**) Strong acoustic streaming can dissociate IgA from saliva mucin proteins. (**B**) Schematic of the portable AIMDx device integrating the sample purification and antibody detection modules. (**C**) Image of a single detection unit consisting of four electrochemical sensors. (**D**) Illustration of an electrochemical sensor containing a working electrode and a counter electrode. (**E** and **F**) Detected background noise and net signal in saliva samples with varying concentrations of IgA ($n = 3$). (**G** and **H**) LOD of IgA antibody with and without on-chip purification ($n = 3$). (**I**) Typical antibody profile versus time, adapted from published work (*67*). (**J** and **K**) Detected net signal of anti-SARS-CoV-2 IgA and IgG antibodies in (J) raw (unpurified) PCR-positive samples and (K) acoustically purified samples ($n = 3$). (**L** to **N**) Detected net signal of anti-SARS-CoV-2 IgA, IgG, and IgM antibodies in clinical samples from eight patients who recovered from Covid and seven healthy controls. (**O**) Using our multiantibody detection device, a three-dimensional representation of host immune profiles for eight patient samples and seven healthy controls. The distinct spatial separation clearly distinguishes healthy samples from patient samples.

labeled W1, W2, W3, and W4, while C represents the counter electrode. The lower right inlet serves as a sheath flow and is used to program the rate at which detection reagents are introduced, while the left outlet serves as a waste outlet. Purified samples are introduced into the sensor through the upper right inlet. An image of one sensing unit is shown in Fig. 4D. Each unit consists of an array of microelectrochemical sensors, and the working electrode is coated with the SARS-CoV-2 spike protein RBD antigen. As the purified saliva sample passes over the sensor, host antibodies (anti-spike-RBD-IgA/IgM/IgG) in the sample bind to the RBD protein. Next, secondary antibody (biotinylated anti-human IgA/IgM/IgG from rabbit) and streptavidin-poly–horseradish peroxidase (poly-HRP) conjugates are

sequentially added to the detection unit. Last, an ELISA 3,3′, 5,5′-tetramethylbenzidine (TMB) solution is added to the detection unit and the amperometric current is measured using a microammeter. The measured current is directly proportional to the concentration of the host anti-SARS-CoV-2 antibody.

Because raw saliva samples contain various impurities, including large cells and microvesicles, they are prone to nonspecific binding during electrochemical sensing. This results in high background noise, which can lead to false positive detection. To address this problem, our device incorporates an acoustofluidic-based sample purification module to remove impurities, thereby reducing background noise and enhancing detection sensitivity and specificity. To demonstrate the efficacy of this approach, we spiked healthy saliva samples with varying concentrations of the anti-SARS-CoV-2 S1 RBD IgA antibody and loaded said samples into the device with and without acoustofluidic purification. We then compared the electrical readout from sensors coated with SARS-CoV-2 spike protein RBD versus uncoated sensors to determine the relative strength of the total signal versus background noise. Figure 4 (E and F) shows the detected background noise and net signal (difference between total signal and background noise) of saliva samples with varying concentrations of IgA with and without on-chip purification. The detected total signal is shown in fig. S9. Background noise is notably reduced, and the net signal is greatly enhanced when acoustic purification is used. To quantify this performance improvement further, we quantified the LOD of host IgA, which we defined as the point at which the total signal exceeds the background noise. Figure 4 (G and H) depicts the LOD of IgA with and without on-chip purification. Without on-chip acoustofluidic purification, the LOD of IgA is 2 ng/ml (at 1 ng/ml, background noise is not distinguishable from the total signal); however, when the sample is acoustically purified on a chip, the LOD can be improved to 15.6 pg/ml, representing a substantial enhancement in detection sensitivity. This is further illustrated in the ratio of total signal to background noise (fig. S9). IgA and IgM are often reported as early detectable antibody biomarkers in COVID-19, with IgA being particularly valuable for indicating disease severity (*62*). However, detecting IgA in noninvasively collected samples, such as saliva, is challenging. This difficulty arises because IgA often appears alongside mucoprotein (*63*).

Figure 4I illustrates the expected COVID-19 IgA, IgG, and IgM antibody levels over time. Comprehensive detection of these antibodies is crucial for early identification of an immune response, which aids in distinguishing active infection from the recovery phase. To demonstrate the early detection capability of our device, we tested eight PCR-positive samples for SARS-CoV-2 IgG and IgA without purification (Fig. 4J) and after acoustofluidic purification (Fig. 4K). All samples showed enhanced signal levels with acoustofluidic purification. For sample S4, neither IgA nor IgG was detected before acoustofluidic purification, while IgA became detectable after acoustofluidic purification. This result indicates that IgA can serve as an early-stage immune biomarker with acoustofluidic purification.

In addition to detecting early immune biomarkers such as IgA, the stability of antibodies during processing is critical for reliable diagnostics. IgM, which is known to be less stable than other antibodies, was validated for stability using electrochemical detection of 16 clinical samples processed with the AIMDx chip. The results showed no notable degradation of IgM under cooling conditions, demonstrating that the device preserves antibody integrity during purification. Moreover, the AIMDx chip exhibited consistent purification performance across different samples, further supporting its robustness and reliability in diverse diagnostic scenarios (fig. S10).

We also tested another 15 clinical samples using our integrated AIMDx device: 8 samples from patients who recovered from SARS-CoV-2 and 7 samples from healthy individuals. The detected net signals of anti-SARS-CoV-2 S1 RBD IgA, IgG, and IgM antibodies in all 15 clinical samples are shown in Fig. 4 (L to N). Clinical samples from healthy individuals exhibit very low (almost negligible) detectable currents for IgA, IgG, and IgM antibodies. Conversely, clinical samples from recovered patients previously exposed to SARS-CoV-2 show high loads of IgA, IgG, and IgM antibodies. The relatively lower detected current associated with IgM detection in some samples from recovered patients may be attributed to lower IgM levels, as IgM tends to be a marker of recent infection, and serum levels of this antibody decrease rapidly over time. In contrast to previous detection methods that can only identify IgG antibodies, our device can simultaneously detect IgA, IgG, and IgM antibodies. This comprehensive approach allows us to identify patients exposed to Covid versus healthy controls. By plotting the detection current for IgA, IgG, and IgM antibodies on the x, y, and z axes in a three-dimensional space, as shown in Fig. 4O, we can visualize the immune profiles of eight patient samples and seven healthy controls. The results are obvious, as healthy samples occupy a distinct region in this three-dimensional space, easily distinguishable from the patient samples. Notably, because of variations in IgM levels, we observed that four of the patients' samples were from the early recovery stage, while the remaining four were from the later recovery stage. This underscores the versatility of our device in tracking and assessing the immune levels of patients and highlights its value for clinical applications. These findings demonstrate that our integrated AIMDx device effectively purifies unprocessed saliva samples containing SARS-CoV-2 viral RNA and host antibodies. Moreover, it enables on-chip simultaneous multiplexed detection, efficiently analyzing multiple antibodies and viral RNA.

DISCUSSION

Nucleic acid testing and immunity protein (antibody) detection are widely used diagnostic tools in tracking population health during outbreaks of infectious diseases. Nucleic acid testing is highly sensitive and can detect a pathogen's genetic material (RNA or DNA), even in the early stages of infection. However, nucleic acid testing can only track current infections and cannot provide information about past infections or immunity. Meanwhile, antibody detection can identify past infection and therefore track disease spread and population immunity; however, it may be unable to determine early infection if a robust antibody response has not yet developed. Recent work has attempted to comprehensively address this issue by combining nucleic acid testing with antibody detection on a single platform to assess infection status and vaccination response (*29*). However, these detection methods typically require either off-chip prepurification of biological fluids or an attempt to use unprocessed saliva or plasma samples. Unfortunately, biological samples, especially saliva, contain debris and large cells, which can create considerable background noise that hinders accurate detection. In addition, these impurities can interfere with protein binding in antibody detection testing or nucleic acid amplification in nucleic acid testing, leading to delays in detecting antibody and viral RNA biomarkers. Last, prior work in the antibody detection space has focused on the

detection of IgG and IgM (*15*, *64*, *65*), which are highly concentrated in biological samples; unfortunately, few studies have explored low-concentration IgA (*66*, *67*), which is an essential biomarker in early infection and an indicator of infection severity.

In this work, we describe a fully integrated acoustic chip that not only purifies raw clinical saliva samples via acoustic vortexes and Gor'kov potential well at a 1/10,000 subwavelength scale in microfluidic channels but also enables the simultaneous detection of viral RNAs and multiple host antibodies with high sensitivity and specificity using RT-LAMP reaction wells and electrochemical sensors. The key innovations of this technology are fourfold. First, we have developed an acoustically oscillating wedge microchannel specifically engineered to trap bacteria, cells, and microvesicles from raw saliva samples to improve downstream detection. Second, we have accomplished the rapid on-chip acoustofluidic lysis of viral particles in saliva samples; this allows us to release viral RNAs efficiently for downstream on-chip detection. Third, we have integrated sample preparation and multiple electrochemical sensors into the device to simultaneously detect IgA, IgG, and IgM antibodies with high detection sensitivity; this allows accurate and comprehensive antibody profiling to track the host immune response. Last, we have seamlessly integrated sample purification, RNA detection, and antibody detection onto a single chip to streamline sample processing and enhance the overall performance of the AIMDx chip.

Prior work has described sample purification methods such as ultracentrifugation, ultrafiltration, and specially designed interdigital transducers (*68*–*70*) for virus and antibody isolation. However, integrating these methods with downstream detection modules on a single chip has been a continued challenge in the field. For instance, ultracentrifugation is associated with the loss of rare antibodies during purification, as these antibodies can mix with mucins and precipitate out of the solution. Meanwhile, the membranes used in ultrafiltration are prone to blockage by food debris in saliva samples, thereby hindering effective sample processing. Last, while high-frequency acoustic systems, such as those using specially designed interdigital transducers, are favored for generating subwavelength potential wells, their rapid attenuation in fluids, nonuniform energy distribution, and reliance on extensive and expensive equipment, such as function generators and amplifiers, pose notable limitations for point-of-care applications. In contrast, our approach uses low-frequency acoustic waves and precisely engineered wedge-shaped microstructures to achieve robust and uniform trapping at larger scales. This design, activated by a 5-kHz acoustic buzzer, efficiently traps debris, cells, and submicrometer vesicles from saliva, overcoming limitations of traditional systems with a portable and cost-effective setup. Future optimizations, such as refining microstructures and incorporating resonators, could further enhance the precision and performance of this technology for biomedical applications (*71*, *72*).

In addition, this acoustofluidic design facilitates rapid on-chip lysis of viral particles. Previous on-chip viral lysis methods have used resistive heaters (*73*, *74*), laser beams (*75*, *76*), and interdigital transducers (*77*, *78*). In contrast, our integrated device requires adding a surfactant solution to purified saliva samples. The acoustic streaming vortexes within the device effectively mix the surfactant with the saliva sample, resulting in rapid lysis. Our design offers a cost-effective and efficient solution for on-chip sample purification and lysis.

Last, the AIMDx chip integrates an RNA detection module and a multiplexed antibody detection module. Together, these allow for the simultaneous detection of multiple targeted SARS-CoV-2 RNAs (N, O, and E) and multiple host antibodies (IgA, IgG, and IgM) from clinical saliva samples. Saliva samples are an excellent substitute for blood samples and nasal swabs, as they are easier to collect and do not require specially trained operators or expensive collection equipment. Furthermore, saliva samples contain both viral RNA and host antibodies, providing information about current infection, prior infection, and vaccination response. The RNA detection module of our AIMDx device consists of four wells to which pre-prepared RT-LAMP mix reagents can be directly added, eliminating the need for RNA extraction kits. This lab-on-chip platform minimizes the number of steps required of the end user to avoid contamination and human error, allowing untrained users to operate the device efficiently and maximizing the chip's value as a point-of-care testing system. Combining the four modules on the AIMDx chip notably enhances the antibody and virus detection capability via the effective processing of saliva samples, allowing for the analysis of low-concentration antibodies at early infection stages. These integrated device features bring promising advanced technology in the rapid, accurate, and comprehensive detection of viral immunoglobulins and nucleic acids that could revolutionize diagnostic approaches during disease outbreaks.

MATERIALS AND METHODS

Design, fabrication, and assembly of integrated AIMDx device

The integrated AIMDx device consists of four modules with distinct functionalities: (i) sample purification, (ii) viral lysis, (iii) detection of RNAs, and (iv) detection of viral immunoglobulins (Fig. 1C). A two-dimensional schematic of the integrated AIMDx device depicting the entire path of the microchannel is shown in fig. S1A. The purification and lysis modules feature 1.2-mm-wide serpentine channels with three turns and wedge microstructures. In the purification module, each row of the microfluidic channel measures 22 mm in length and contains 40 identical tilted wedge microstructures on its sidewall (20 on each side). In the lysis module, each row of the microfluidic channel measures 11 mm in length and contains 18 identical tilted wedge microstructures on its sidewall (9 on each side). Figure S1B provides a detailed zoom view of a small section of a microchannel showcasing six wedge microstructures. These microstructures have a distinctive design with a bottom edge measuring 0.2 mm and a sloping edge extending to 0.5 mm. The sharp edges are angled at 45° along the channel and are uniformly spaced at 1-mm intervals. The antibody detection module comprises three chambers equipped with inlet and outlet ports to facilitate sample flow. Last, the RNA detection module consists of four circular wells, each with a diameter of 2 mm.

The electrochemical sensor contains an array of working and counter electrodes (fig. S1C). Figure S1D shows a detailed zoom view of the electrodes. A ring-shaped counter electrode with an outer diameter of 80 μm surrounds each circular 40-μm-diameter working electrode. The electrodes are uniformly spaced on a rectangular grid at 90-μm-length and 200-μm-width intervals.

A glass wafer (50 mm by 45 mm) was spin coated with positive photoresist SPR3012 to fabricate the electrochemical sensors. Standard photolithography techniques were used to pattern the sensor electrodes onto the wafer. Next, electron beam evaporation deposited a 5-nm chrome layer and a 50-nm gold layer onto the wafer. The excess photoresist was dissolved and removed using a liftoff process to realize the final sensor design.

To fabricate the microfluidic channels, a silicon wafer was spin coated with negative photoresist SU-8 50, and the microchannel designs were patterned onto the wafer using photolithography. PDMS microfluidic channels were obtained using the resultant SU-8 mold through a mold-replica process. Inlet/outlet holes and the four wells used for RNA detection were created using hole punches (World Precision Instruments, US).

The fabricated glass wafer with sensor electrodes was bonded with the PDMS microchannel following a 6-min treatment in an oxygen plasma cleaner and cured at 65°C for 24 hours to achieve complete device assembly. An acoustic buzzer (no. 668-1407-ND, Digikey) was adhered to the bottom of the glass wafer using a thin layer of epoxy (PermaPoxy 5 Minute General Purpose, Permatex).

As the integrated AIMDx device combines both antibody detection and RNA detection modules to enable diverse detection functions on a single chip, minimizing any potential interference between these two modules is crucial. Two microfluidic valves were introduced at the initial microchannel junctions of both the RNA and antibody detection modules to address this issue. The fabrication process of this device with microfluidic control valves is detailed in fig. S11. Through precise control of these microfluidic valves, the sample flow can be effectively regulated to permit or obstruct sample entry into the antibody and RNA detection modules. Detailed information about the designed microfluidic valves and their functions can be found in fig. S12.

Numerical simulation

Finite element simulations were conducted using COMSOL Multiphysics commercial software to investigate the normalized acoustic streaming velocities generated by the vibration of a wedge microstructure. A two-dimensional cross-sectional model of the microchannel in the *x*-*y* plane, featuring five pairs of wedge microstructures, was established. The material inside the channel was defined as water. A thermoviscous acoustic module and frequency-domain analysis were used to obtain an initial solution. The displacement has in-plane and out-of-plane components. However, the out-of-plane components are nearly constant over short channel heights (50 μm) and do not result in acoustic streaming. Therefore, only the in-plane displacement was considered. The wavelength of the acoustic wave is 0.3 m, which is orders of magnitude larger than the wedge microstructure geometry and channel. Therefore, the background displacement can be written as $d = d_0 e^{i\omega t}$, where d_0 is the amplitude of the in-plane displacement. To calculate the acoustic field, a background acoustic vibration velocity was introduced at the left end of the channel (fig. S13A). The right end of the channel was set to a prescribed pressure of 0 Pa. The model is calculated at a frequency of 5 kHz in the Frequency Domain Solver. The acoustic vibration velocity will change around the tip of the wedge microstructure (fig. S13B). The acoustic Gor'kov potential (*79*) is calculated from the pressure p and acoustic vibration velocity v (v_x, v_y) via

$$U = V_p\left(\frac{f_1}{2\rho_0 {c_0}^2} < p \cdot p^* > - \frac{3}{4}\rho_0 f_2 < v \cdot v^* >\right) \quad (1)$$

$$f_1 = 1 - \frac{\rho_0 {c_0}^2}{\rho_p {c_p}^2} \quad (2)$$

$$f_2 = \frac{2(\rho_p - \rho_0)}{(2\rho_p + \rho_0)} \quad (3)$$

where $\rho_0 = 1$ g/cm^3, $c_0 = 1500$ m/s, $\rho_p = 1.04$ g/cm^3, and $c_p = 2320$ m/s are the density and speed of sound in water and particles, respectively. V_p is the volume of a particle with a diameter of 100 nm, and $< >$ is the time average operator.

To calculate acoustic streaming in the microfluidic channel, a body force $\boldsymbol{F}$ (F_x, F_y) is applied to the laminar flow module (*80*)

$$F_x = \frac{\rho_0}{2} < Re\left[{v_x}^* \, d(v_x, x) + {v_y}^* \, d(v_x, y)\right] \quad (4)$$

$$F_y = \frac{\rho_0}{2} < Re\left[{v_x}^* \, d(v_y, x) + {v_y}^* \, d(v_y, y)\right] \quad (5)$$

The left end is set to the flow inlet with $v_x = 0.5$ mm/s, and the right end is set to the outlet. The main challenge of the acoustic streaming calculation is the convergence of the module with a Stationary solver, as acoustic streaming is a nonlinear phenomenon. Therefore, a time-dependent solver better fits the requirements. To help the module converge, we first calculated the Stationary results without the body force described above as an initial value of a time-dependent solver. The time-dependent solver starts at time $t = 0$ and ends at $t = T$, with a step of $T/50$, where T is the period of the acoustic waves. The acoustic streaming velocity distribution is calculated by averaging the flow velocity in a period. Longer times T were also calculated, but no apparent changes were observed.

Image acquisition and analysis

Images and movies of particle trajectories were obtained using an upright microscope (Olympus, Japan) coupled with a charge-coupled device camera (Photometrics, US). Movies were recorded at a frame rate of 100 frames/s. To create the particle tracing figure (Fig. 2E), frames were selected at 10-frame intervals and overlaid. The green fluorescent polystyrene particles used in the experiment were purchased from Magsphere, US.

Western blot and ELISA analysis

To compare the concentrations of mucoprotein and α-amylase in the raw (unpurified) versus purified saliva samples, equal volumes (60 μl) of each sample were collected. SDS-polyacrylamide gel electrophoresis was used for protein separation. The proteins were transferred onto a polyvinylidene fluoride membrane (Bio-Rad, US). The membrane was incubated overnight at 4°C with primary antibody (anti-salivary alpha amylase antibody and recombinant anti-Mucin 5 AC antibody, Abcam, UK). Next, the membrane was exposed to an appropriate HRP-conjugated secondary antibody (goat anti-rabbit IgG, Abcam, UK) for 1 hour at room temperature. Last, protein expression levels were imaged using a ChemiDoc XRS+ imaging system (Bio-Rad, US).

The concentration of whole IgG in the raw (unpurified) versus purified saliva samples was quantified using a standard Human IgG ELISA kit (no. ab195215, Abcam, UK). Before analysis, the samples were diluted 5000× with Sample Diluent NS from the kit. The detection sensitivity for anti-SARS-CoV-2 S1 RBD IgA antibody by a standard COVID-19 S1 RBD protein human IgA ELISA kit (no. IEQ-CoVS1RBD-IgA, RayBiotech, US) was also quantified in raw (unpurified) versus purified saliva samples. For this analysis, anti-SARS-CoV-2 S1 RBD IgA antibody (no. srbd-mab6, InvivoGen, US) was added to untreated saliva from healthy controls. The samples were then passed through the device with (purified) and without (unpurified) acoustics

and diluted 30× using the sample diluent from the standard kit. To detect the total signal and background noise, 96-well microplates coated with SARS-CoV-2 S1 RBD protein and albumin were used for ELISA. The results of Fig. 2K were determined by calculating the net RBD-attributable signal, which was obtained by subtracting the background noise from the total signal.

TEM imaging

The virus sample was prepared by diluting inactivated SARS-CoV-2 whole virus pellet (no. 76460-364, VWR, US) into 100 μl of molecular standard water and mixing with an equal volume of 0.1× TAE buffer (no. B49, Thermo Fisher Scientific, US). The virus sample, along with the lysis buffer, was then passed through the lysis module of the device, both with and without acoustic lysis. Samples were then collected for TEM imaging. Briefly, TEM samples were prepared by placing a 30 μl droplet of the sample on a Parafilm (VWR, US) sheet, followed by transfer to a 300-mesh copper grid support film (Electron Microscopy Sciences, US) over 20 min. The grid was washed three times with 30 μl of distilled water for 2 min. Last, the grid was left to dry at room temperature, and the sample was imaged using an FEI Tecnai G2 Twin microscope (FEI Company, US).

Saliva sample preparation

After obtaining informed consent from participants and receiving approval from the institutional review board at the University of California, Los Angeles, saliva samples were collected from healthy individuals (IRB no. 06-07-018-11), symptomatic patients (IRB no. 20-000473), and patients who recovered from COVID-19 (IRB no. 20-000500). These samples were carefully pipetted into cryotubes for storage at −80°C. Heat-inactivated SARS-CoV-2 virus (American Type Culture Collection, US) was introduced into saliva samples from healthy controls at the desired concentrations to generate samples spiked with the virus. Similarly, to create samples spiked with antibodies, anti-SARS-CoV-2 S1 RBD IgA antibody (no. srbd-mab6, InvivoGen, US) was added to samples from healthy controls at the desired concentrations.

RT-LAMP assay

The heat-inactivated SARS-CoV-2 virus (no. NR52286, isolate: USA-WA1/2020) was purchased from BEI (American Type Culture Collection) with a total concentration of 1.77×10^8 genome equivalents/ml. The mixed RT-LAMP reagents were prepared following the manufacturer's instructions. Briefly, RT-LAMP 2X Master Mix (no. M1804, New England Biolabs) and primers (1.6 μM forward inner primer, 1.6 μM backward inner primer, 0.2 μM F3, 0.2 μM B3, 0.4 μM Loop F, and 0.4 μM Loop B) were combined in ultrapure distilled water (no. 2646316, Invitrogen). Primer sequences for the three targets (N, E, and O genes of SARS-CoV-2) are described in table S1.

For each RT-LAMP assay, virus samples were prepared by directly spiking the virus into saliva samples from healthy controls to achieve the desired concentration. The virus samples were loaded into the inlet of the device and passed through the purification channel of the integrated device. Upon reaching the lysis channel, a mixture of 0.1× TAE buffer (no. B49, Thermo Fisher Scientific, US) and 10% Tween 20 was combined with the virus sample at a ratio of 5:5:1 (v/v/v) virus sample:TAE buffer:Tween 20, both to facilitate lysis and to stabilize the obtained viral RNA sample. The previously prepared RT-LAMP reagents were added when the purified and lysed samples reached the RNA detection module. Using a thermoelectric cooler, the reaction was then incubated at 65°C for 30 min per the manufacturer's recommendation.

To quantify the colorimetric readout of the RT-LAMP reaction, spectrophotometric optical density (OD) was measured using a NanoDrop machine (no. 13-400-525, Thermo Fisher Scientific, US). The color value obtained after the RT-LAMP reaction was determined by calculating the difference in absorbance at the two wavelengths exhibiting the maximum absorption in phenol red ($\Delta OD = OD_{430\ nm} - OD_{560\ nm}$). A threshold of $\Delta OD > +1$ was used to classify samples as positive for SARS-CoV-2 RNA on the basis of RT-LAMP.

Electrochemical sensing

Electrochemical sensing was used to detect SARS-CoV-2 viral RNA and host anti-SARS-CoV-2 antibodies. The product from the RT-LAMP reaction was retrieved after sample purification, viral RNA extraction, and on-chip RT-LAMP processes using the AIMDx chip. Electrochemical sensing assays were then conducted to detect viral RNA. Restrictive enzyme digestion was performed using four endonucleases (Hae II, Hinc II, Bco DI, and Pst I) from New England Biolabs to facilitate detection. Thirty-microliter reaction mixtures were prepared, consisting of 3 μl of 10× Cutsmart Buffer, 0.5 μl of Hae II, 0.5 μl of Hinc II, 0.5 μl of Pst I, 1 μl of Bco DI, 19.5 μl of water, and 5 μl of the product obtained from the RT-LAMP reaction. The mixture was then incubated at 37°C for 15 min. As previously described, the amplified and digested N targets were subsequently determined using electric field–induced release and measurement assays (*81*).

Electrochemical sensing assays for antibody detection were performed in five distinct steps: (i) protein immobilization, (ii) primary antibody binding, (iii) secondary antibody binding, (iv) streptavidin-poly-HRP conjugate binding, and (v) signal readout.

Protein immobilization

A protein immobilization master mix (MM) was prepared by combining 5 μl of pyrrole (no. W338605, Sigma-Aldrich, US) and 50 μl of 3 M potassium chloride (no. 60137, Sigma-Aldrich, US) in 940 μl of ultrapure water (no. 10-977-015, Thermo Fisher Scientific, US). MM with RBD was prepared by adding 33.71 μl of SARS-CoV-2 spike protein RBD (no. Z03483-1, Genscript, US) to 996.29 μl of MM. MM without RBD was prepared by mixing 995 μl of MM and 5 μl of ultrapure water. Electrodes on the glass substrate were precoated with either MM with RBD or MM without RBD by applying a voltage of 1.1 V for 1 s, followed by a voltage of 0.35 V for 1 s for four cycles. The electrodes are washed with wash buffer (1× phosphate-buffered saline with 0.05% Tween 20) for 3 min.

Antibody binding

Saliva samples were loaded into the channel to fill the antibody detection chamber. The sample was incubated in the device for 10 min at room temperature to allow any detection antibody (anti-SARS-CoV-2 S1 RBD IgA/IgM/IgG) present in the sample to bind to the RBD protein. The chamber was then washed with wash buffer for 3 min.

Secondary antibody binding

Biotinylated rabbit anti-human IgA (no. 31-1030-02, RevMAb Biosciences, US) was diluted in Blocker Casein (no. 37528, Thermo Fisher Scientific, US) at a 1:800 (v/v) ratio. Similarly, biotinylated goat anti-human IgG (no. 13-4998-83, Invitrogen, US) and biotinylated goat anti-human IgM (no. 31778, Invitrogen, US) were diluted in Blocker Casein at a 1:400 (v/v) ratio. The prepared anti-human IgA/IgG/IgM biotinylated antibodies were loaded into the corresponding

chambers and incubated at room temperature for 10 min to bind the primary detection antibody. The chamber was then washed with wash buffer for 3 min.

Streptavidin-poly-HRP conjugate binding

Streptavidin-poly-HRP conjugate (no. 65R-S122, Fitzgerald, US) was diluted in Blocker Casein at a 1:5 (v/v) ratio. The diluted conjugate was added to each chamber and incubated for 10 min to bind the secondary antibody. Subsequently, the sample was washed with a wash buffer for 3 min.

Signal readout

For electrochemical signal readout, a 1-Step TMB ELISA substrate solution (no. 34028, Thermo Fisher Scientific, US) was added to each chamber. Following a 1-min incubation at room temperature, the amperometric current in each chamber was read on the developed sensing module of an integrated printed circuit board (fig. S14) by applying a −0.2-V current to the electrodes for 1 min.

Supplementary Materials

The PDF file includes:

Figs. S1 to S14
Table S1
Legends for movies S1 to S3

Other Supplementary Material for this manuscript includes the following:

Movies S1 to S3

REFERENCES AND NOTES

1. D. M. Morens, J. K. Taubenberger, Pandemic influenza: Certain uncertainties. *Rev. Med. Virol.* **21**, 262–284 (2011).
2. M. E. Nickol, J. Kindrachuk, A year of terror and a century of reflection: Perspectives on the great influenza pandemic of 1918–1919. *BMC Infect. Dis.* **19**, 117 (2019).
3. M. K. Annavajhala, H. Mohri, P. Wang, M. Nair, J. E. Zucker, Z. Sheng, A. Gomez-Simmonds, A. L. Kelley, M. Tagliavia, Y. Huang, Emergence and expansion of SARS-CoV-2 B.1.526 after identification in New York. *Nature* **597**, 703–708 (2021).
4. Y. J. Hou, S. Chiba, P. Halfmann, C. Ehre, M. Kuroda, K. H. Dinnon III, S. R. Leist, A. Schäfer, N. Nakajima, K. Takahashi, SARS-CoV-2 D614G variant exhibits efficient replication ex vivo and transmission in vivo. *Science* **370**, 1464–1468 (2020).
5. V. M. Kadiri, C. Bussi, A. W. Holle, K. Son, H. Kwon, G. Schutz, M. G. Gutierrez, P. Fischer, Biocompatible magnetic micro- and nanodevices: Fabrication of FePt nanopropellers and cell transfection. *Adv. Mater.* **32**, e2001114 (2020).
6. W. R. de Araujo, H. Lukas, M. D. T. Torres, W. Gao, C. de la Fuente-Nunez, Low-cost biosensor technologies for rapid detection of COVID-19 and future pandemics. *ACS Nano* **18**, 1757–1777 (2024).
7. R. Wölfel, V. M. Corman, W. Guggemos, M. Seilmaier, S. Zange, M. A. Müller, D. Niemeyer, T. C. Jones, P. Vollmar, C. Rothe, M. Hoelscher, T. Bleicker, S. Brünink, J. Schneider, R. Ehmann, K. Zwirglmaier, C. Drosten, C. Wendtner, Virological assessment of hospitalized patients with COVID-2019. *Nature* **581**, 465–469 (2020).
8. S. Cao, Y. Gan, C. Wang, M. Bachmann, S. Wei, J. Gong, Y. Huang, T. Wang, L. Li, K. Lu, H. Jiang, Y. Gong, H. Xu, X. Shen, Q. Tian, C. Lv, F. Song, X. Yin, Z. Lu, Post-lockdown SARS-CoV-2 nucleic acid screening in nearly ten million residents of Wuhan, China. *Nat. Commun.* **11**, 5917 (2020).
9. M. N. Esbin, O. N. Whitney, S. Chong, A. Maurer, X. Darzacq, R. Tjian, Overcoming the bottleneck to widespread testing: A rapid review of nucleic acid testing approaches for COVID-19 detection. *RNA* **26**, 771–783 (2020).
10. H. Lee, W. Wang, N. Chauhan, Y. Xiong, N. Magazine, O. Valdescruz, D. Y. Kim, T. Qiu, W. Huang, X. Wang, Rapid detection of intact SARS-CoV-2 using designer DNA Nets and a pocket-size smartphone-linked fluorimeter. *Biosens. Bioelectron.* **229**, 115228 (2023).
11. S. Lee, J. S. Park, H. Woo, Y. K. Yoo, D. Lee, S. Chung, D. S. Yoon, K.-B. Lee, J. H. Lee, Rapid deep learning-assisted predictive diagnostics for point-of-care testing. *Nat. Commun.* **15**, 1695 (2024).
12. M. García-Fiñana, I. E. Buchan, Rapid antigen testing in COVID-19 responses. *Science* **372**, 571–572 (2021).
13. J. Dinnes, P. Sharma, S. Berhane, S. S. van Wyk, N. Nyaaba, J. Domen, M. Taylor, J. Cunningham, C. Davenport, S. Dittrich, D. Emperador, L. Hooft, M. M. Leeflang, M. D. McInnes, R. Spijker, J. Y. Verbakel, Y. Takwoingi, S. Taylor-Phillips, A. Van den Bruel, J. J. Deeks, Cochrane COVID-19 Diagnostic Test Accuracy Group, Rapid, point-of-care antigen tests for diagnosis of SARS-CoV-2 infection. *Cochrane Database Syst. Rev.* **7**, CD013705 (2022).
14. C. Gaebler, Z. Wang, J. C. C. Lorenzi, F. Muecksch, S. Finkin, M. Tokuyama, A. Cho, M. Jankovic, D. Schaefer-Babajew, T. Y. Oliveira, M. Cipolla, C. Viant, C. O. Barnes, Y. Bram, G. Breton, T. Hägglöf, P. Mendoza, A. Hurley, M. Turroja, K. Gordon, K. G. Millard, V. Ramos, F. Schmidt, Y. Weisblum, D. Jha, M. Tankelevich, G. Martinez-Delgado, J. Yee, R. Patel, J. Dizon, C. Unson-O'Brien, I. Shimeliovich, D. F. Robbiani, Z. Zhao, A. Gazumyan, R. E. Schwartz, T. Hatziioannou, P. J. Bjorkman, S. Mehandru, P. D. Bieniasz, M. Caskey, M. C. Nussenzweig, Evolution of antibody immunity to SARS-CoV-2. *Nature* **591**, 639–644 (2021).
15. H. Hou, T. Wang, B. Zhang, Y. Luo, L. Mao, F. Wang, S. Wu, Z. Sun, Detection of IgM and IgG antibodies in patients with coronavirus disease 2019. *Clin. Transl. Immunology* **9**, e01136 (2020).
16. T. Fox, J. Geppert, J. Dinnes, K. Scandrett, J. Bigio, G. Sulis, D. Hettiarachchi, Y. Mathangasinghe, P. Weeratunga, D. Wickramasinghe, H. Bergman, B. S. Buckley, K. Probyn, Y. Sguassero, C. Davenport, J. Cunningham, S. Dittrich, D. Emperador, L. Hooft, M. M. Leeflang, M. D. McInnes, R. Spijker, T. Struyf, A. Van den Bruel, J. Y. Verbakel, Y. Takwoingi, S. Taylor-Phillips, J. J. Deeks, Antibody tests for identification of current and past infection with SARS-CoV-2. *Cochrane Database Syst. Rev.* **2022**, CD013652 (2022).
17. M. Teymouri, S. Mollazadeh, H. Mortazavi, Z. N. Ghale-Noie, V. Keyvani, F. Aghababaei, M. R. Hamblin, G. Abbaszadeh-Goudarzi, H. Pourghadamyari, S. M. R. Hashemian, Recent advances and challenges of RT-PCR tests for the diagnosis of COVID-19. *Pathol. Res. Pract.* **221**, 153443 (2021).
18. S. Jegerlehner, F. Suter-Riniker, P. Jent, P. Bittel, M. Nagler, Diagnostic accuracy of a SARS-CoV-2 rapid antigen test in real-life clinical settings. *Int. J. Infect. Dis.* **109**, 118–122 (2021).
19. J. Zhao, Q. Yuan, H. Wang, W. Liu, X. Liao, Y. Su, X. Wang, J. Yuan, T. Li, J. Li, S. Qian, C. Hong, F. Wang, Y. Liu, Z. Wang, Q. He, Z. Li, B. He, T. Zhang, Y. Fu, S. Ge, L. Liu, J. Zhang, N. Xia, Z. Zhang, Antibody responses to SARS-CoV-2 in patients with novel coronavirus disease 2019. *Clin. Infect. Dis.* **71**, 2027–2034 (2020).
20. J. E. Kong, Q. Wei, D. Tseng, J. Zhang, E. Pan, M. Lewinski, O. B. Garner, A. Ozcan, D. Di Carlo, Highly stable and sensitive nucleic acid amplification and cell-phone-based readout. *ACS Nano* **11**, 2934–2943 (2017).
21. P. Zhang, X. Zhou, M. He, Y. Shang, A. L. Tetlow, A. K. Godwin, Y. Zeng, Ultrasensitive detection of circulating exosomes with a 3D-nanopatterned microfluidic chip. *Nat. Biomed. Eng.* **3**, 438–451 (2019).
22. A. Ganguli, A. Mostafa, J. Berger, M. Y. Aydin, F. Sun, S. A. S. d. Ramirez, E. Valera, B. T. Cunningham, W. P. King, R. Bashir, Rapid isothermal amplification and portable detection system for SARS-CoV-2. *Proc. Natl. Acad. Sci. U.S.A.* **117**, 22727–22735 (2020).
23. S. Chen, Y. Sun, F. Fan, S. Chen, Y. Zhang, Y. Zhang, X. Meng, J.-M. Lin, Present status of microfluidic PCR chip in nucleic acid detection and future perspective. *TrAC Trend. Anal. Chem.* **157**, 116737 (2022).
24. S. Park, Y. Zhang, S. Lin, T.-H. Wang, S. Yang, Advances in microfluidic PCR for point-of-care infectious disease diagnostics. *Biotechnol. Adv.* **29**, 830–839 (2011).
25. J. Reboud, Y. Bourquin, R. Wilson, G. S. Pall, M. Jiwaji, A. R. Pitt, A. Graham, A. P. Waters, J. M. Cooper, Shaping acoustic fields as a toolset for microfluidic manipulations in diagnostic technologies. *Proc. Natl. Acad. Sci. U.S.A.* **109**, 15162–15167 (2012).
26. N. L. Welch, M. Zhu, C. Hua, J. Weller, M. E. Mirhashemi, T. G. Nguyen, S. Mantena, M. R. Bauer, B. M. Shaw, C. M. Ackerman, S. G. Thakku, M. W. Tse, J. Kehe, M.-M. Uwera, J. S. Eversley, D. A. Bielwaski, G. McGrath, J. Braidt, J. Johnson, F. Cerrato, G. K. Moreno, L. A. Krasilnikova, B. A. Petros, G. L. Gionet, E. King, R. C. Huard, S. K. Jalbert, M. L. Cleary, N. A. Fitzgerald, S. B. Gabriel, G. R. Gallagher, S. C. Smole, L. C. Madoff, C. M. Brown, M. W. Keller, M. M. Wilson, M. K. Kirby, J. R. Barnes, D. J. Park, K. J. Siddle, C. T. Happi, D. T. Hung, M. Springer, B. L. MacInnis, J. E. Lemieux, E. Rosenberg, J. A. Branda, P. C. Blainey, P. C. Sabeti, C. Myhrvold, Multiplexed CRISPR-based microfluidic platform for clinical testing of respiratory viruses and identification of SARS-CoV-2 variants. *Nat. Med.* **28**, 1083–1094 (2022).
27. Y. Chen, S. Qian, X. Yu, J. Wu, J. Xu, Microfluidics: The propellant of CRISPR-based nucleic acid detection. *Trend. Biotechnol.* **41**, 557–574 (2023).
28. R. Bruch, J. Baaske, C. Chatelle, M. Meirich, S. Madlener, W. Weber, C. Dincer, G. A. Urban, CRISPR/Cas13a-powered electrochemical microfluidic biosensor for nucleic acid amplification-free miRNA diagnostics. *Adv. Mater.* **31**, e1905311 (2019).
29. D. Najjar, J. Rainbow, S. Sharma Timilsina, P. Jolly, H. de Puig, M. Yafia, N. Durr, H. Sallum, G. Alter, J. Z. Li, X. G. Yu, D. R. Walt, J. A. Paradiso, P. Estrela, J. J. Collins, D. E. Ingber, A lab-on-a-chip for the concurrent electrochemical detection of SARS-CoV-2 RNA and anti-SARS-CoV-2 antibodies in saliva and plasma. *Nat. Biomed. Eng.* **6**, 968–978 (2022).
30. J. Aleman, T. Kilic, L. S. Mille, S. R. Shin, Y. S. Zhang, Microfluidic integration of regeneratable electrochemical affinity-based biosensors for continual monitoring of organ-on-a-chip devices. *Nat. Protoc.* **16**, 2564–2593 (2021).
31. A. Bekdemir, F. Stellacci, A centrifugation-based physicochemical characterization method for the interaction between proteins and nanoparticles. *Nat. Commun.* **7**, 13121 (2016).

32. M. L. Heinemann, M. Ilmer, L. P. Silva, D. H. Hawke, A. Recio, M. A. Vorontsova, E. Alt, J. Vykoukal, Benchtop isolation and characterization of functional exosomes by sequential filtration. *J. Chromatogr. A* **1371**, 125–135 (2014).
33. K. Fung, Y. Li, S. Fan, A. K. Fajrial, Y. Ding, X. Ding, Acoustically excited microstructure for on-demand fouling mitigation in a microfluidic membrane filtration device. *J. Membr. Sci. Lett.* **2**, 100012 (2022).
34. S. Nagrath, L. V. Sequist, S. Maheswaran, D. W. Bell, D. Irimia, L. Ulkus, M. R. Smith, E. L. Kwak, S. Digumarthy, A. Muzikansky, Isolation of rare circulating tumour cells in cancer patients by microchip technology. *Nature* **450**, 1235–1239 (2007).
35. W. Su, X. Gao, L. Jiang, J. Qin, Microfluidic platform towards point-of-care diagnostics in infectious diseases. *J. Chromatogr. A* **1377**, 13–26 (2015).
36. J. Lamanna, E. Y. Scott, H. S. Edwards, M. D. Chamberlain, M. D. Dryden, J. Peng, B. Mair, A. Lee, C. Chan, A. A. Sklavounos, Digital microfluidic isolation of single cells for -Omics. *Nat. Commun.* **11**, 5632 (2020).
37. R. Eivazzadeh-Keihan, H. Bahreinizad, Z. Amiri, H. A. M. Aliabadi, M. Salimi-Bani, A. Nakisa, F. Davoodi, B. Tahmasebi, F. Ahmadpour, F. Radinekiyan, A. Maleki, M. R. Hamblin, M. Mahdavi, H. Madanchi, Functionalized magnetic nanoparticles for the separation and purification of proteins and peptides. *TrAC Trend. Anal. Chem.* **141**, 116291 (2021).
38. Z. Wang, S. Ahmed, M. Labib, H. Wang, L. Wu, F. Bavaghar-Zaeimi, N. Shokri, S. Blanco, S. Karim, K. Czarnecka-Kujawa, E. H. Sargent, A. J. R. McGray, M. de Perrot, S. O. Kelley, Isolation of tumour-reactive lymphocytes from peripheral blood via microfluidic immunomagnetic cell sorting. *Nat. Biomed. Eng.* **7**, 1188–1203 (2023).
39. Y. Wan, G. Cheng, X. Liu, S.-J. Hao, M. Nisic, C.-D. Zhu, Y.-Q. Xia, W.-Q. Li, Z.-G. Wang, W.-L. Zhang, Rapid magnetic isolation of extracellular vesicles via lipid-based nanoprobes. *Nat. Biomed. Eng.* **1**, 0058 (2017).
40. J. Friend, L. Y. Yeo, Microscale acoustofluidics: Microfluidics driven via acoustics and ultrasonics. *Rev. Mod. Phys.* **83**, 647–704 (2011).
41. H. Bruus, J. Dual, J. Hawkes, M. Hill, T. Laurell, J. Nilsson, S. Radel, S. Sadhal, M. Wiklund, Forthcoming Lab on a Chip tutorial series on acoustofluidics: Acoustofluidics—Exploiting ultrasonic standing wave forces and acoustic streaming in microfluidic systems for cell and particle manipulation. *Lab Chip* **11**, 3579–3580 (2011).
42. D. J. Collins, B. Morahan, J. Garcia-Bustos, C. Doerig, M. Plebanski, A. Neild, Two-dimensional single-cell patterning with one cell per well driven by surface acoustic waves. *Nat. Commun.* **6**, 8686 (2015).
43. M. Wu, A. Ozcelik, J. Rufo, Z. Wang, R. Fang, T. Jun Huang, Acoustofluidic separation of cells and particles. *Microsyst. Nanoeng.* **5**, 32 (2019).
44. Y. Gu, C. Chen, Z. Mao, H. Bachman, R. Becker, J. Rufo, Z. Wang, P. Zhang, J. Mai, S. Yang, J. Zhang, S. Zhao, Y. Ouyang, D. T. W. Wong, Y. Sadovsky, T. J. Huang, Acoustofluidic centrifuge for nanoparticle enrichment and separation. *Sci. Adv.* **7**, eabc0467 (2021).
45. J. Zhang, C. Chen, R. Becker, J. Rufo, S. Yang, J. Mai, P. Zhang, Y. Gu, Z. Wang, Z. Ma, J. Xia, N. Hao, Z. Tian, D. T. W. Wong, Y. Sadovsky, L. P. Lee, T. J. Huang, A solution to the biophysical fractionation of extracellular vesicles: Acoustic Nanoscale Separation via Wave-pillar Excitation Resonance (ANSWER). *Sci. Adv.* **8**, eade0640 (2022).
46. J. Xia, Z. Wang, R. Becker, F. Li, F. Wei, S. Yang, J. Rich, K. Li, J. Rufo, J. Qian, K. Yang, C. Chen, Y. Gu, R. Zhong, P. J. Lee, D. T. W. Wong, L. P. Lee, T. J. Huang, Acoustofluidic virus isolation via bessel beam excitation separation technology. *ACS Nano* **18**, 22596–22607 (2024).
47. P. Zhang, H. Bachman, A. Ozcelik, T. J. Huang, Acoustic microfluidics. *Annu. Rev. Anal. Chem.* **13**, 17–43 (2020).
48. H. Zhang, A. Li, K. Li, Z. Wang, X. Xu, Y. Wang, M. V. Sheridan, H.-S. Hu, C. Xu, E. V. Alekseev, Z. Zhang, P. Yan, K. Cao, Z. Chai, T. E. Albrecht-Schönzart, S. Wang, Ultrafiltration separation of Am(VI)-polyoxometalate from lanthanides. *Nature* **616**, 482–487 (2023).
49. J. Zhang, L. T. H. Nguyen, R. Hickey, N. Walters, X. Wang, K. J. Kwak, L. J. Lee, A. F. Palmer, E. Reátegui, Immunomagnetic sequential ultrafiltration (iSUF) platform for enrichment and purification of extracellular vesicles from biofluids. *Sci. Rep.* **11**, 8034 (2021).
50. S. Y. Leong, H. B. Ong, H. M. Tay, F. Kong, M. Upadya, L. Gong, M. Dao, R. Dalan, H. W. Hou, Microfluidic size exclusion chromatography (μSEC) for extracellular vesicles and plasma protein separation. *Small* **18**, e2104470 (2022).
51. A. N. Böing, E. van der Pol, A. E. Grootemaat, F. A. W. Coumans, A. Sturk, R. Nieuwland, Single-step isolation of extracellular vesicles by size-exclusion chromatography. *J. Extracell. Ves.* **3**, 23430 (2014).
52. N. Herrmann, P. Neubauer, M. Birkholz, Spiral microfluidic devices for cell separation and sorting in bioprocesses. *Biomicrofluidics* **13**, 061501 (2019).
53. J.-H. Lee, S.-K. Lee, J.-H. Kim, J.-H. Park, Separation of particles with bacterial size range using the control of sheath flow ratio in spiral microfluidic channel. *Sens. Actuators A. Phys.* **286**, 211–219 (2019).
54. P. Dumčius, R. Mikhaylov, X. Zhang, M. Bareford, M. Stringer, R. Errington, C. Sun, E. Gonzalez, T. Krukovski, J. M. Falcon-Perez, D. Liang, Y.-Q. Fu, A. Clayton, X. Yang, Dual-wave acoustofluidic centrifuge for ultrafast concentration of nanoparticles and extracellular vesicles. *Small* **19**, e2300390 (2023).
55. W. Witkowska McConnell, C. Davis, S. R. Sabir, A. Garrett, A. Bradley-Stewart, P. Jajesniak, J. Reboud, G. Xu, Z. Yang, R. Gunson, Paper microfluidic implementation of loop mediated isothermal amplification for early diagnosis of hepatitis C virus. *Nat. Commun.* **12**, 6994 (2021).
56. D. McCloskey, A. Semeere, R. Ayanga, M. Laker-Oketta, R. Lukande, M. Semakadde, M. Kanyesigye, M. Wenger, P. LeBoit, T. McCalmont, LAMP-enabled diagnosis of Kaposi's sarcoma for sub-Saharan Africa. *Sci. Adv.* **9**, eadc8913 (2023).
57. L. P. Guaman-Bautista, E. Moreta-Urbano, C. G. Oña-Arias, M. Torres-Arias, N. C. Kyriakidis, K. Malcı, N. Jonguitud-Borrego, L. Rios-Solis, E. Ramos-Martinez, A. López-Cortés, C. Barba-Ostria, Tracking SARS-CoV-2: Novel trends and diagnostic strategies. *Diagnostics* **11**, 1981 (2021).
58. Z. Ma, A. W. Holle, K. Melde, T. Qiu, K. Poeppel, V. M. Kadiri, P. Fischer, Acoustic holographic cell patterning in a biocompatible hydrogel. *Adv. Mater.* **32**, e1904181 (2020).
59. Z. Gong, M. Baudoin, Three-dimensional trapping and assembly of small particles with synchronized spherical acoustical vortices. *Phys. Rev. Appl.* **14**, 064002 (2020).
60. A. Marzo, M. Caleap, B. W. Drinkwater, Acoustic virtual vortices with tunable orbital angular momentum for trapping of Mie particles. *Phys. Rev. Lett.* **120**, 044301 (2018).
61. A. Del Campo Fonseca, C. Glück, J. Droux, Y. Ferry, C. Frei, S. Wegener, B. Weber, M. El Amki, D. Ahmed, Ultrasound trapping and navigation of microrobots in the mouse brain vasculature. *Nat. Commun.* **14**, 5889 (2023).
62. Y. X. Chao, O. Rötzschke, E. K. Tan, The role of IgA in COVID-19. *Brain Behav. Immun.* **87**, 182–183 (2020).
63. H. L. Gibbins, G. B. Proctor, G. E. Yakubov, S. Wilson, G. H. Carpenter, SIgA binding to mucosal surfaces is mediated by mucin-mucin interactions. *PLOS ONE* **10**, e0119677 (2015).
64. Q. Lin, D. Wen, J. Wu, L. Liu, W. Wu, X. Fang, J. Kong, Microfluidic immunoassays for sensitive and simultaneous detection of IgG/IgM/antigen of SARS-CoV-2 within 15 min. *Anal. Chem.* **92**, 9454–9458 (2020).
65. T. Liu, J. Hsiung, S. Zhao, J. Kost, D. Sreedhar, C. V. Hanson, K. Olson, D. Keare, S. T. Chang, K. P. Bliden, P. A. Gurbel, U. S. Tantry, J. Roche, C. Press, J. Boggs, J. P. Rodriguez-Soto, J. G. Montoya, M. Tang, H. Dai, Quantification of antibody avidities and accurate detection of SARS-CoV-2 antibodies in serum and saliva on plasmonic substrates. *Nat. Biomed. Eng.* **4**, 1188–1196 (2020).
66. M. Chen, R. Qin, M. Jiang, Z. Yang, W. Wen, J. Li, Clinical applications of detecting IgG, IgM or IgA antibody for the diagnosis of COVID-19: A meta-analysis and systematic review. *Int. J. Infect. Dis.* **104**, 415–422 (2021).
67. H. Ma, W. Zeng, H. He, D. Zhao, D. Jiang, P. Zhou, L. Cheng, Y. Li, X. Ma, T. Jin, Serum IgA, IgM, and IgG responses in COVID-19. *Cell. Mol. Immunol.* **17**, 773–775 (2020).
68. J. Rufo, F. Cai, J. Friend, M. Wiklund, T. J. Huang, Acoustofluidics for biomedical applications. *Nat. Rev. Methods Primers* **2**, 30 (2022).
69. S. Yang, Z. Tian, Z. Wang, J. Rufo, P. Li, J. Mai, J. Xia, H. Bachman, P.-H. Huang, M. Wu, Harmonic acoustics for dynamic and selective particle manipulation. *Nat. Mater.* **21**, 540–546 (2022).
70. S. Yang, J. Rufo, R. Zhong, J. Rich, Z. Wang, L. P. Lee, T. J. Huang, Acoustic tweezers for high-throughput single-cell analysis. *Nat. Protoc.* **18**, 2441–2458 (2023).
71. J. Rufo, P. Zhang, R. Zhong, L. P. Lee, T. J. Huang, A sound approach to advancing healthcare systems: the future of biomedical acoustics. *Nat. Commun.* **13**, 3459 (2022).
72. M. Wu, Z. Ma, Z. Tian, J. T. Rich, X. He, J. Xia, Y. He, K. Yang, S. Yang, K. W. Leong, L. P. Lee, T. J. Huang, Sound innovations for biofabrication and tissue engineering. *Micosyst. Nanoeng.* **10**, 170 (2024).
73. N. Privorotskaya, Y.-S. Liu, J. Lee, H. Zeng, J. A. Carlisle, A. Radadia, L. Millet, R. Bashir, W. P. King, Rapid thermal lysis of cells using silicon–diamond microcantilever heaters. *Lab Chip* **10**, 1135–1141 (2010).
74. L. A. Marshall, L. L. Wu, S. Babikian, M. Bachman, J. G. Santiago, Integrated printed circuit board device for cell lysis and nucleic acid extraction. *Anal. Chem.* **84**, 9640–9645 (2012).
75. A. M. Kaba, H. Jeon, A. Park, K. Yi, S. Baek, A. Park, D. Kim, Cavitation-microstreaming-based lysis and DNA extraction using a laser-machined polycarbonate microfluidic chip. *Sens. Actuators B. Chem.* **346**, 130511 (2021).
76. S.-H. Huang, L.-Y. Hung, G.-B. Lee, Continuous nucleus extraction by optically-induced cell lysis on a batch-type microfluidic platform. *Lab Chip* **16**, 1447–1456 (2016).
77. Z. Wang, P.-H. Huang, C. Chen, H. Bachman, S. Zhao, S. Yang, T. J. Huang, Cell lysis via acoustically oscillating sharp edges. *Lab Chip* **19**, 4021–4032 (2019).
78. D. Taller, K. Richards, Z. Slouka, S. Senapati, R. Hill, D. B. Go, H.-C. Chang, On-chip surface acoustic wave lysis and ion-exchange nanomembrane detection of exosomal RNA for pancreatic cancer study and diagnosis. *Lab Chip* **15**, 1656–1666 (2015).
79. L. P. Gor'kov, in *Soviet Physics Doklady* (World Scientific Publishing Co., 1962), vol. 6, pp. 773–775.
80. C. Zhang, X. Guo, L. Royon, P. Brunet, Unveiling of the mechanisms of acoustic streaming induced by sharp edges. *Phys. Rev. E* **102**, 043110 (2020).
81. M. Tu, J. Cheng, Y. L. Chen, W. C. Jea, W. L. Chen, C. J. Chen, C. L. Ho, W. L. Huang, C. C. Lin, W. C. Su, Q. Ye, J. Deignan, W. Grody, F. Li, D. Chia, F. Wei, W. Liao, D. T. W. Wong, C. M. Strom, Electric field-induced release and measurement (EFIRM): Characterization and technical validation of a novel liquid biopsy platform in plasma and saliva. *J. Mol. Diagn.* **22**, 1050–1062 (2020).

Acknowledgments: We acknowledge support from the Shared Materials Instrumentation Facility (SMIF) at Duke University. **Funding:** The authors acknowledge support from the

National Institutes of Health (U18TR003778, R01AG084098, R01GM141055, R01HD103727, R01GM143439, R01GM145960, R01GM144417, R44OD024963, R44AG063643, R44GM154514, and R44GM154515) and National Science Foundation (CMMI-2104295). **Author contributions:** J.Q., J.X., and T.J.H. conceived the idea. J.Q. and J.X. fabricated the devices and performed all the experiments, numerical simulations, and data analysis. S.C., F.L., F.W., and M.A. designed the electrochemical sensing method and performed the experiments. V.G. and J.M. designed and tested the circuit board. J.Q., J.X., J.F.L., K.L., R.Z., Y.H., K.Y., L.P.L., and T.J.H. contributed to the scientific presentation. Y.K. and O.O.Y. coordinated the sample collection and transfer. All the authors contributed to manuscript preparation and editing. D.T.W.W., L.P.L., and T.J.H. provided overall guidance. **Competing interests:** T.J.H. has cofounded a start-up company, Ascent Bio-Nano Technologies Inc., to commercialize technologies involving acoustofluidics and acoustic tweezers. At the time of the research, D.T.W.W. had equity in Liquid Diagnostics LLC and RNAmeTRIX Inc. All other authors declare that they have no competing interests. **Data and materials availability:** All data needed to evaluate the conclusions in the paper are present in the paper and/or the Supplementary Materials. No special code was developed for this project.

Submitted 14 October 2024
Accepted 16 December 2024
Published 15 January 2025
10.1126/sciadv.adt5464